

COMPARISON AND ERROR MODELING OF VELOCITY-BASED INITIAL ORBIT DETERMINATION ALGORITHMS

Linyi Hou^{*}, Kevin Lohan[†], and Zachary R. Putnam[‡]

Recently, Christian and Hollenberg proposed and solved a new class of initial orbit determination problems based only on velocity measurements.^{1,2} We introduce a modification to the velocity-based initial orbit determination algorithm to improve accuracy and computational efficiency. Orbit determination error trends with respect to semi-major axis, eccentricity, initial true anomaly, and sensor noise are modeled using the orbit hodograph, and verified using Monte Carlo simulations. An example is provided to show that error trend models can accurately predict the error of hodograph-based velocity initial orbit determination algorithms.

INTRODUCTION

Initial orbit determination (IOD) is the process of determining the orbit of an object in space from a set of measurements, with no a priori knowledge of the orbit itself. IOD methods typically rely on measurements of the object's position. Methods by Laplace, Gauss, and Gooding all require at least three measurements of the object's angular position.³⁻⁷ Gibbs' method solves the IOD problem with three position vectors.^{5,6} Lambert's method requires two position vectors and the time of flight between those two positions.³

Past IOD methods leveraged measurements from available technology of the time; with the development of new sensing techniques, more types of measurement data have become available, calling for the development of novel IOD techniques. Velocity-based initial orbit determination (VIOD) is a new class of IOD problem recently proposed and solved by Christian and Hollenberg.^{1,2} Their work was inspired by the development of x-ray pulsar navigation (XNAV), an in-space navigation technique based on observing stable millisecond x-ray pulsars. XNAV sensors can provide near-inertial velocity measurements without the need for position information.⁸

Principally, VIOD relies on the measurement of three or more inertial velocity vectors to determine the orbit of an object by finding corresponding position vectors. While Christian and Hollenberg have developed two algorithms for solving the VIOD problem,^{1,2} little analysis has been performed to compare and assess these algorithms in terms of accuracy and computational efficiency. Understanding VIOD performance is the first step to determining its utility.

This paper establishes a framework to model VIOD error trends using the orbit hodograph. First, an improved VIOD algorithm is proposed and compared against previously developed algorithms. Next, VIOD error trends are analytically modeled. Then, the model is verified using Monte Carlo simulations. Finally, an example is provided to demonstrate the application of the error model.

^{*}Undergraduate Student, Department of Aerospace Engineering, University of Illinois at Urbana-Champaign, Urbana, IL

[†]Ph.D. Student, Department of Aerospace Engineering, University of Illinois at Urbana-Champaign, Urbana, IL

[‡]Assistant Professor, Department of Aerospace Engineering, University of Illinois at Urbana-Champaign, Urbana, IL.

REVIEW OF VIOD ALGORITHMS

Christian and Hollenberg previously introduced two different VIOD algorithms,^{1,2} which this paper shall refer to as the “energy method” and the “hodograph method”. Their solution approaches are outlined in the subsections below. A review of the orbit hodograph is provided. An improved version of the hodograph method is then proposed and outlined.

The Energy Method

The “energy method” proposed by Christian and Hollenberg¹ utilizes the conservation of momentum and the vis-viva equation to construct a linear system and solve the VIOD problem. The solution process is summarized below.

Observe that three given velocity vectors $\{\mathbf{v}_1, \mathbf{v}_2, \mathbf{v}_3\}$ must lie on the same orbital plane. In the presence of noise, a least-squares approach can be used to determine the orbital plane that best fits the velocity vectors. Construct the matrix \mathbf{N} :

$$\mathbf{N} = [\mathbf{v}_1, \mathbf{v}_2, \mathbf{v}_3]^T \quad (1)$$

The unit vector \mathbf{k} orthogonal to the orbital plane can be found by taking the singular value decomposition (SVD) $\mathbf{N} = \mathbf{U}\mathbf{D}\mathbf{V}^T$ and selecting the column in \mathbf{V} corresponding to the smallest singular value in \mathbf{D} . With the orientation of the orbital plane defined, construct Eqs. (2)-(5):

$$\mathbf{u}_i = \frac{\mathbf{v}_i}{\|\mathbf{v}_i\|} \quad , \quad \mathbf{w}_i = \frac{\mathbf{u}_i \times \mathbf{k}}{\|\mathbf{u}_i \times \mathbf{k}\|} \quad (2)$$

$$\mathbf{r}_{u_i} = (\mathbf{u}_i \mathbf{u}_i^T) \mathbf{r}_i \quad , \quad \mathbf{r}_{w_i} = (\mathbf{w}_i \mathbf{w}_i^T) \mathbf{r}_i \quad (3)$$

$$\mathbf{h} = \mathbf{r} \times \mathbf{v} \quad , \quad \mathbf{z}_i = \frac{1}{\|\mathbf{v}_i\|} \mathbf{w}_i \quad (4)$$

$$\alpha_i = \frac{\mu}{\|\mathbf{r}_i\|} \quad , \quad \beta_i = \gamma_i \frac{\mu}{\|\mathbf{r}_i\|} \frac{\|\mathbf{r}_{u_i}\|}{\|\mathbf{h}\|} \quad (5)$$

where $\gamma_i = \pm 1$ such that $\mathbf{r}_{u_i} = \gamma_i \|\mathbf{r}_{u_i}\| \mathbf{u}_i$. Define the vector \mathbf{g} :

$$\mathbf{g} = [\alpha_1 \ \beta_1 \ \alpha_2 \ \beta_2 \ \alpha_3 \ \beta_3]^T \quad (6)$$

A linear system may now be constructed:

$$\begin{bmatrix} \mathbf{z}_1 & \mathbf{u}_1 & -\mathbf{z}_2 & -\mathbf{u}_2 & \mathbf{0}_{3 \times 1} & \mathbf{0}_{3 \times 1} \\ \mathbf{z}_1 & \mathbf{u}_1 & \mathbf{0}_{3 \times 1} & \mathbf{0}_{3 \times 1} & -\mathbf{z}_3 & -\mathbf{u}_3 \\ \mathbf{0}_{3 \times 1} & \mathbf{0}_{3 \times 1} & \mathbf{z}_2 & \mathbf{u}_2 & -\mathbf{z}_3 & -\mathbf{u}_3 \\ 1 & 0 & -1 & 0 & 0 & 0 \\ 1 & 0 & 0 & 0 & -1 & 0 \\ 0 & 0 & 1 & 0 & -1 & 0 \end{bmatrix} \mathbf{g} = \begin{bmatrix} \|\mathbf{v}_1\| \mathbf{w}_1 - \|\mathbf{v}_2\| \mathbf{w}_2 \\ \|\mathbf{v}_1\| \mathbf{w}_1 - \|\mathbf{v}_3\| \mathbf{w}_3 \\ \|\mathbf{v}_2\| \mathbf{w}_2 - \|\mathbf{v}_3\| \mathbf{w}_3 \\ \|\mathbf{v}_1\|^2/2 - \|\mathbf{v}_2\|^2/2 \\ \|\mathbf{v}_1\|^2/2 - \|\mathbf{v}_3\|^2/2 \\ \|\mathbf{v}_2\|^2/2 - \|\mathbf{v}_3\|^2/2 \end{bmatrix} \quad (7)$$

Solving for \mathbf{g} then leads to the position vector $\tilde{\mathbf{r}}_i$ via Eqs. (8)-(11):

$$\|\tilde{\mathbf{r}}_i\| = \frac{\mu}{\alpha_i} \quad (8)$$

$$\mathbf{r}_{w_i} = h\mathbf{z}_i \quad (9)$$

$$\mathbf{r}_{u_i} = \frac{\beta_i h \|\tilde{\mathbf{r}}_i\|}{\mu} \mathbf{u}_i \quad (10)$$

$$\tilde{\mathbf{r}}_i = \mathbf{r}_{w_i} + \mathbf{r}_{u_i} \quad (11)$$

Further details of the solution process can be found in Reference 1. The linear system shown in Eq. (7) can accommodate more than three velocity measurements by including all unique $\{i, j\}$ pairs and expanding the matrices accordingly.

Review of the Orbit Hodograph

A brief review of the orbit hodograph is provided before the discussion of VIOD algorithms based on the hodograph. Consider a spacecraft in orbit about a central body. All velocity vectors measured in orbit can be plotted from the origin to form a circle known as the hodograph. The hodograph has radius R and its center is offset from the origin by c , with $c = eR$ where e is the eccentricity of the orbit. The true anomaly spanned by velocity measurements is Δf .

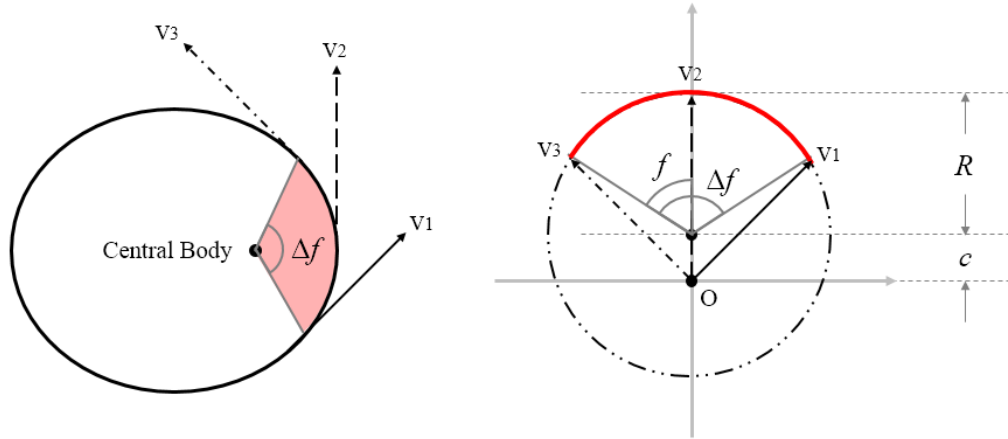


Figure 1. Velocity measurements taken along the orbit are mapped onto the hodograph. Solid ellipse: spacecraft orbit (left). Dot-dash circle: orbit hodograph (right).

The Hodograph Method

The “hodograph method” introduced by Hollenberg and Christian² applies circle fitting to the velocity hodograph to solve the VIOD problem.

Using the same approach as the energy method, obtain the unit vector \mathbf{k} normal to the orbital plane. Next, define a new reference frame (the “orbital” frame) for the velocity vectors, where the z -axis is aligned with \mathbf{k} , and the x -axis is perpendicular to both \mathbf{v}_1 and \mathbf{k} , as shown in Eq. (12). The rotation matrix to this new reference frame is given by \mathbf{T}_O^I , defined in Eq. (13).

$$\mathbf{u}_x = \frac{\mathbf{v}_1 \times \mathbf{k}}{\|\mathbf{v}_1 \times \mathbf{k}\|} \quad (12)$$

$$\mathbf{T}_O^I = [\mathbf{u}_x, \mathbf{u}_y, \mathbf{k}]^T \quad (13)$$

Now, the measurements $\{\mathbf{v}_1, \dots, \mathbf{v}_n\}$ can be converted to the orbital frame with Eq. (14). Note that $\dot{z}_{O_i} \approx 0$ when the measurement noise is small.

$$[\dot{x}_{O_i}, \dot{y}_{O_i}, \dot{z}_{O_i}]^T = \mathbf{T}_O^I \mathbf{v}_i \quad (14)$$

Subsequently, a linear system may be constructed as shown by Eq. (15):

$$\begin{bmatrix} 2\dot{x}_{O_1} & 2\dot{y}_{O_1} & 1 \\ \vdots & \vdots & \vdots \\ 2\dot{x}_{O_n} & 2\dot{y}_{O_n} & 1 \end{bmatrix} \begin{bmatrix} \dot{x}_c \\ \dot{y}_c \\ g \end{bmatrix} = \begin{bmatrix} \dot{x}_{O_1}^2 + \dot{y}_{O_1}^2 \\ \vdots \\ \dot{x}_{O_n}^2 + \dot{y}_{O_n}^2 \end{bmatrix} \quad (15)$$

where (\dot{x}_c, \dot{y}_c) is the center of the hodograph, and the hodograph radius can be found using Eq. (16):

$$R = \sqrt{\dot{x}_c^2 + \dot{y}_c^2 - g} \quad (16)$$

The coordinates of the hodograph center and the eccentricity vector in the inertial frame are:

$$\mathbf{c} = [\mathbf{T}_O^I]^T \begin{bmatrix} \dot{x}_c \\ \dot{y}_c \\ 0 \end{bmatrix} \quad (17)$$

$$\mathbf{e} = \frac{\mathbf{c}}{R} \times \mathbf{k} \quad (18)$$

Finally, construct the following vector components

$$\mathbf{u}_{\perp_i} = \frac{\mathbf{v}_i - \mathbf{c}}{\|\mathbf{v}_i - \mathbf{c}\|} \quad (19)$$

$$\mathbf{u}_{\parallel_i} = \frac{\mathbf{v}_i - \mathbf{c}}{\|\mathbf{v}_i - \mathbf{c}\|} \times \mathbf{k} \quad (20)$$

$$\mathbf{v}_{\perp_i} = (\mathbf{u}_{\perp_i} \mathbf{u}_{\perp_i}^T) \mathbf{v}_i \quad (21)$$

which can be assembled into the position vector via Eqs. (22)-(23).

$$\rho_i = \frac{\mu \|\mathbf{e} + \mathbf{u}_{\parallel_i}\|}{\|\mathbf{v}_{\perp_i}\| \|\mathbf{v}_i\|} \quad (22)$$

$$\tilde{\mathbf{r}}_i = \rho_i \mathbf{u}_{\parallel_i} \quad (23)$$

The hodograph method can similarly be extended for more than three measurements by expanding Eq. (15) to accommodate additional data. Further details on the implementation of this algorithm can be found in Reference 2.

THE IMPROVED HODOGRAPH METHOD

This paper proposes an improvement to the hodograph method by replacing the circle fitting algorithm used to find the orbit hodograph. The original algorithm in Eq. (15) is known as the Kåsa fit. The Kåsa fit produces results biased toward small circles when given data points sampled from short arcs.^{9,10} The accuracy of this process may be improved by using the “hyperaccurate” fit, which eliminates essential bias to achieve a more accurate fit.⁹ The essential bias is the second-highest-order term in the bias of the circle fitting parameter estimates.

The hyperaccurate circle fitting algorithm begins by defining a circle with the equation

$$A(x^2 + y^2) + Bx + Cy + D = 0. \quad (24)$$

Let $\mathbf{A} = (A, B, C, D)$, and define the data matrix \mathbf{Z} and matrix of moments \mathbf{M} :

$$\mathbf{Z} \triangleq [\mathbf{z}, \mathbf{x}, \mathbf{y}, \mathbf{1}] , \quad \mathbf{M} \triangleq \frac{1}{n} \mathbf{Z}^T \mathbf{Z} \quad (25)$$

where $\mathbf{x} = [x_1, \dots, x_n]^T$, $\mathbf{y} = [y_1, \dots, y_n]^T$, and $z_i = x_i^2 + y_i^2$. The circle fitting problem becomes a problem of solving the unconstrained minimization:

$$\mathcal{G}(\mathbf{A}, \eta) = \mathbf{A}^T \mathbf{M} \mathbf{A} - \eta (\mathbf{A}^T \mathbf{N} \mathbf{A} - 1) \quad (26)$$

where η is the Lagrange multiplier and

$$\mathbf{N} = \begin{bmatrix} 8\bar{z} & 4\bar{x} & 4\bar{y} & 2 \\ 4\bar{x} & 1 & 0 & 0 \\ 4\bar{y} & 0 & 1 & 0 \\ 2 & 0 & 0 & 0 \end{bmatrix} \quad (27)$$

The hyperaccurate circle fitting algorithm (implemented in MATLAB) used in this paper was adapted from a C++ implementation in Reference 11. The hyperaccurate circle fitting algorithm replaces the Kåsa fit in the original hodograph method, as shown in the overview of hodograph-based VIOD algorithms in Table 1. Furthermore, the circle fitting quality of the Kåsa fit and the hyperaccurate fit are compared in Figure 2, showing that for points sampled from short arcs in (b), the hyperaccurate fit produces a circle much closer to the original than the Kåsa fit does.

Table 1. A high-level overview of hodograph-based VIOD algorithms.

Step	Original	Improved
1	Use SVD to find orbit plane	
2	Use Kåsa fit to find hodograph	Use hyperaccurate fit to find hodograph
3	Find position from hodograph using Eqs. (18)-(23)	

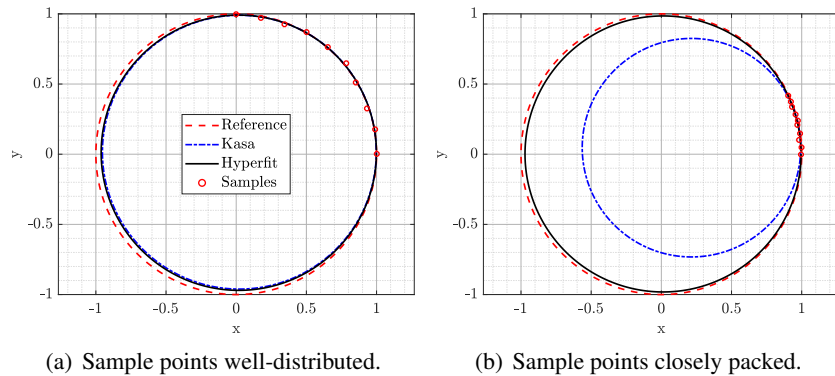


Figure 2. The performance of the Kåsa fit and the hyperaccurate fit are compared for points sampled from (a) a long arc and (b) a short arc.

METHODOLOGY

Throughout this paper, Monte Carlo simulation is used to examine VIOD error in the presence of measurement noise. In this section, the models used for orbit simulation and sensor noise are outlined, along with definitions for canonical units and VIOD error.

Orbit Simulation

A spacecraft in two-body motion is assumed for orbit simulations:

$$\frac{d^2}{dt^2}\mathbf{r} = -\frac{\mu}{\|\mathbf{r}\|^3}\mathbf{r} \quad (28)$$

where \mathbf{r} is the position vector of the spacecraft relative to the central body and μ is the gravitational parameter of the central body. The spacecraft's position and velocity can then be expressed analytically at any point in the orbit using the Keplerian elements $\{a, e, i, \Omega, \omega, f\}$. A visual representation of the Keplerian elements is shown in Figure 3.

$$\begin{aligned} \mathbf{r} = & r(\cos \Omega \cos \theta - \sin \Omega \sin \theta \cos i) \hat{\mathbf{I}} \\ & + r(\sin \Omega \cos \theta + \cos \Omega \sin \theta \cos i) \hat{\mathbf{J}} \\ & + r \sin \theta \sin i \hat{\mathbf{K}} \end{aligned} \quad (29)$$

$$\begin{aligned} \mathbf{v} = & -\frac{\mu}{h}[\cos \Omega(\sin \theta + e \sin \omega) + \sin \Omega(\cos \theta + e \cos \omega) \cos i] \hat{\mathbf{I}} \\ & -\frac{\mu}{h}[\sin \Omega(\sin \theta + e \sin \omega) - \cos \Omega(\cos \theta + e \cos \omega) \cos i] \hat{\mathbf{J}} \\ & +\frac{\mu}{h}(\cos \theta + e \cos \omega) \sin i \hat{\mathbf{K}} \end{aligned} \quad (30)$$

where $\theta = \omega + f$, $r = \|\mathbf{r}\|$, and h is the specific angular momentum of the spacecraft:

$$r = \frac{a(1 - e^2)}{1 + e \cos f} \quad (31)$$

$$h = \sqrt{\mu a(1 - e^2)} \quad (32)$$

The spacecraft orbit is defined using the Keplerian elements, and the spacecraft states \mathbf{r}, \mathbf{v} are propagated analytically using Eqs. (29)-(32) by propagating the true anomaly f . The true anomaly is found by solving Kepler's equation in Eq. (33) using Newton's method, and then solving Eq. (34):

$$M = E - e \sin E \quad (33)$$

$$\tan \frac{E}{2} = \left(\frac{1 - e}{1 + e} \right)^{1/2} \tan \frac{f}{2} \quad (34)$$

where M is the mean anomaly and E is the eccentric anomaly. To obtain M for a time t since periapsis passage, one simply computes $M = t\sqrt{\mu/a^3}$.

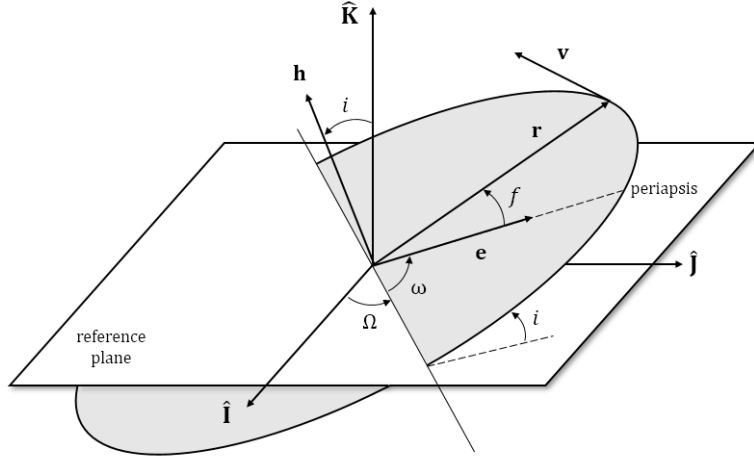


Figure 3. The Keplerian orbit elements. Adapted from Prussing and Conway, Figure 3.3.³

Sensor Noise Model

With the truth position and velocity vectors defined by two-body orbital mechanics, simulated sensor noise can then be added to the velocity measurements. Sensor noise magnitude is modeled by a zero-mean normal distribution with standard deviation σ . The direction of the sensor noise unit vector $\hat{\eta}$ is randomly generated. Given the normal distribution function $\mathcal{N}(\mu, \sigma^2)$ where μ is the mean and σ is the standard deviation, the sensor noise η is then:

$$\eta = \mathcal{N}(0, \sigma^2) \hat{\eta} \quad (35)$$

subsequently, the i -th noisy velocity measurement $\tilde{\mathbf{v}}_i$ can be calculated using Eq. (36). For each velocity measurement, a new, random sensor noise η is generated. It is assumed that each sensor noise vector is independent.

$$\tilde{\mathbf{v}}_i = \mathbf{v}_i + \eta_i \quad (36)$$

Canonical Units

Canonical units are used throughout this paper to standardize simulation results. Canonical units are constructed by defining the distance unit, DU, using the semi-major axis of the orbit of interest:

$$\mu \triangleq 1 \cdot \frac{DU^3}{TU^2} \quad , \quad a \triangleq 1 \times 10^5 \text{ DU} \quad (37)$$

where DU is the canonical distance unit, TU is the canonical time unit, a is the semi-major axis, and μ is the gravitational parameter of the central body. It follows that

$$DU = a \cdot 10^{-5} \quad , \quad TU = \sqrt{DU^3/\mu} \quad (38)$$

Error Evaluation

The accuracy of VIOD algorithms is assessed with the relative root mean square error (RMSE) of the position vector of the first measurement. Let $\text{RMSE}(\tilde{\mathbf{r}})$ be the relative RMSE between the

calculated position from VIOD, $\tilde{\mathbf{r}}$, and the spacecraft's true position in space, \mathbf{r} . Over n simulations, the relative RMSE error of position is defined as:

$$\text{RMSE}(\tilde{\mathbf{r}}) = \sqrt{\frac{1}{n} \sum_i^n \frac{\|\tilde{\mathbf{r}}_i - \mathbf{r}\|}{\|\mathbf{r}\|}} \quad (39)$$

COMPARISON OF VIOD ALGORITHMS

The energy method, hodograph method, and improved hodograph method were compared in the context of both VIOD accuracy and computation time. A 3000-sample Monte Carlo simulation was performed with $\mu = 1$ and Keplerian elements $a = 1 \times 10^5$ DU, $e = 0.5$, $i = \Omega = \omega = 0^\circ$, and $f = 160^\circ$. 20 measurements are taken over 10% of the orbit period at equal time intervals with the sensor noise standard deviation $\sigma = 3 \times 10^{-6}$ DU/TU. This equates to measuring in Low Earth Orbit (LEO) with $a = 7200$ km for 10 minutes with a sensor noise standard deviation of 7.1 m/s.

Accuracy

The accuracy of the three VIOD methods relative to two-body mechanics were assessed by independently varying the noise standard deviation σ , eccentricity e , and initial true anomaly f_0 . The results are shown in Figure 4.

The improved method is significantly more accurate when σ is large, e is high, or f_0 is near π . The energy method is comparable with the hodograph method in most cases but becomes worse at high eccentricities. Furthermore, the RMSE for the improved hodograph method appears to be linear as a function of σ , whereas the RMSE of the other two methods grow at a higher rate than $\mathcal{O}(\sigma)$. This is consistent with the fact that the “hyperaccurate” circle fit used by the improved hodograph method has no essential bias (the highest order error term), meaning the improve hodograph method should have a lower order of error growth rate.

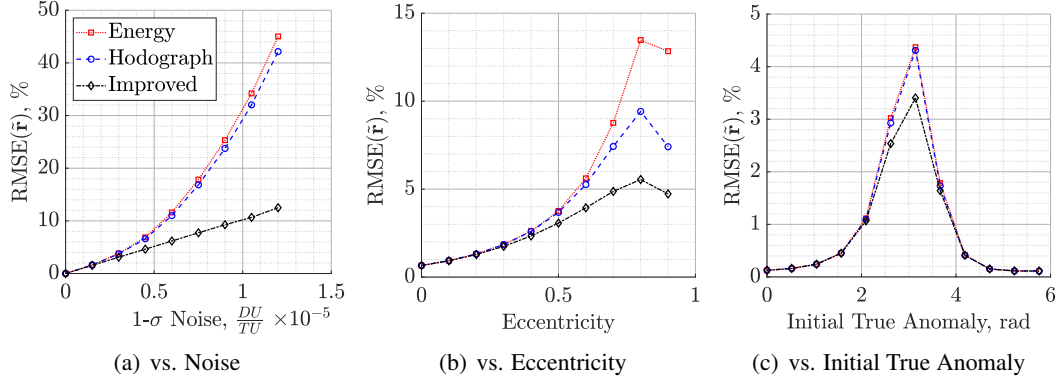


Figure 4. Comparison of $\text{RMSE}(\tilde{\mathbf{r}})$ between 3 VIOD methods as a function of a) sensor noise standard deviation, b) eccentricity, and c) initial true anomaly.

Computation Time

The computation time required to evaluate 1000 Monte Carlo samples for each algorithm as a function of the number of velocity measurements is tabulated in Table 2 and shown in Figure 5.

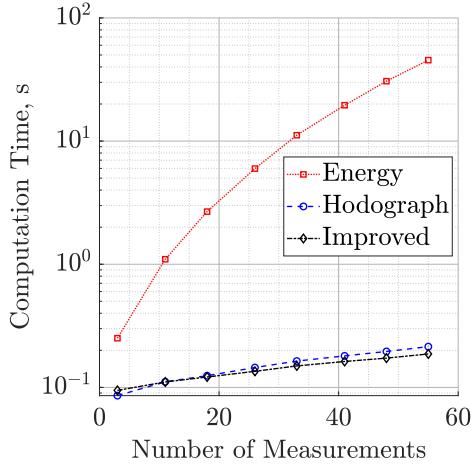


Figure 5. VIOD computation time comparison.

Table 2. Tabulated computation times.

#	Energy	Hodograph	Improved
3	0.251 s	0.0857 s	0.0946 s
11	1.10 s	0.111 s	0.111 s
18	2.67 s	0.124 s	0.121 s
26	5.98 s	0.145 s	0.135 s
33	11.2 s	0.164 s	0.149 s
41	19.5 s	0.180 s	0.162 s
48	30.6 s	0.196 s	0.173 s
55	45.4 s	0.214 s	0.187 s

The hodograph method is significantly faster than the energy method. This is expected since the linear system of the energy method scales poorly with more measurements, as is discussed by Christian and Hollenberg.² The improved hodograph method is only slightly faster than the hodograph method. This difference is not necessarily indicative of algorithm efficiency. Instead, the difference likely reflects the specific implementation of each algorithm in software, which was not optimized for.

Summary

The improved method outperforms previous VIOD methods both in terms of accuracy and computation speed, making it the clear candidate for further analysis among the three methods presented. In the next section, VIOD (using the the improved method) is assessed in greater depth, and an analytic error trend model is developed.

ERROR MODELING FOR THE IMPROVED HODOGRAPH METHOD

Since the improved hodograph method is based on fitting velocity measurements to the orbit hodograph, analyzing the orbit hodograph may reveal mechanisms by which VIOD error develops. This section identifies these mechanisms and analytically models their impact on the estimate of the hodograph radius, \tilde{R} .

A critical assumption is made in the error model that the relative RMSE for \tilde{R} is proportional to $\text{RMSE}(\tilde{\mathbf{r}})$, as shown in Eq. (40). To validate this assumption, $\text{RMSE}(\tilde{\mathbf{r}})$ and $\text{RMSE}(\tilde{R})$ are compared with respect to several parameters that influence the orbit hodograph, as shown in Figure 6.

$$\text{RMSE}(\tilde{\mathbf{r}}) \propto \text{RMSE}(\tilde{R}) \quad (40)$$

All subplots shown in Figure 6 are derived from a baseline case: the orbit is defined with $a = 1 \times 10^5$ DU, $e = 0.5$, and $f_0 = 90^\circ$; 10 measurements are taken over 10% of the orbit period at equal time intervals with sensor noise $\sigma = 3 \times 10^{-6}$ DU/TU.

To produce each subplot in Figure 6, a single parameter is varied while other parameters are held constant. For each new parameter value, a 3000-sample Monte Carlo simulation is performed.

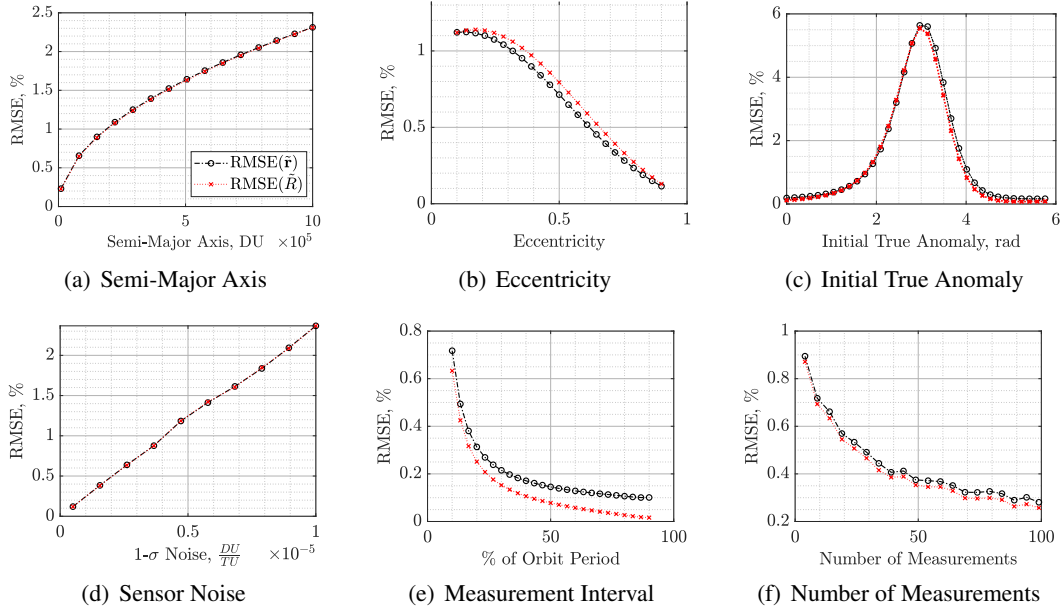


Figure 6. $\text{RMSE}(\tilde{\mathbf{r}})$ is compared against $\text{RMSE}(\tilde{R})$ with respect to a , e , f_0 , σ , the measurement interval, and the number of measurements.

The hodograph radius error, $\text{RMSE}(\tilde{R})$, is scaled such that the range of error values equals that of $\text{RMSE}(\tilde{\mathbf{r}})$. The error trend in hodograph radius closely resembles the error trends of VIOD for variations in the semi-major axis, eccentricity, initial true anomaly, and sensor noise.

However, there is a distinct offset between $\text{RMSE}(\tilde{R})$ and $\text{RMSE}(\tilde{\mathbf{r}})$ when varying the measurement interval and the number of measurements. In certain cases, the difference is even greater, making $\text{RMSE}(\tilde{R})$ a poor predictor of $\text{RMSE}(\tilde{\mathbf{r}})$. In Figure 7, a new baseline case with $e = 0.9$, $f_0 = 0^\circ$, and $\sigma = 3 \times 10^{-4}$ DU/TU is used, showing that the error trends for $\tilde{\mathbf{r}}$ and \tilde{R} do not match under certain conditions. In (a), $\text{RMSE}(\tilde{R})$ diverges from $\text{RMSE}(\tilde{\mathbf{r}})$. In (b), while the trends are similar in shape, $\text{RMSE}(\tilde{R})$ is offset to a much greater value than $\text{RMSE}(\tilde{\mathbf{r}})$.

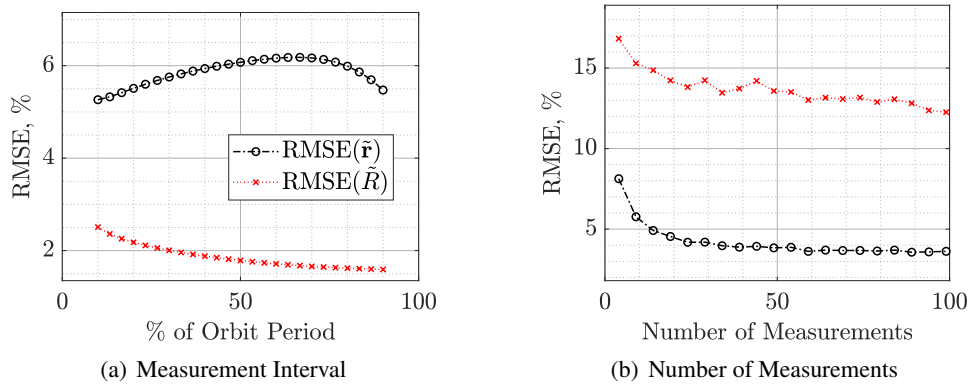


Figure 7. $\text{RMSE}(\tilde{\mathbf{r}})$ is compared against $\text{RMSE}(\tilde{R})$ with respect to the measurement interval and the number of measurements.

In summary, $\text{RMSE}(\tilde{R})$ is proportional to $\text{RMSE}(\tilde{\mathbf{r}})$ with respect to the semi-major axis, eccentricity, initial true anomaly, and sensor noise standard deviation. It is therefore possible to use a model of hodograph radius error to predict VIOD error trends with respect to these variables.

Scaling is required for $\text{RMSE}(\tilde{R})$ to equal $\text{RMSE}(\tilde{\mathbf{r}})$, therefore the models developed in this section can only reflect $\text{RMSE}(\tilde{\mathbf{r}})$ trends, but not specific values for any particular case. However, if $\text{RMSE}(\tilde{\mathbf{r}})$ is known for any case, the error trend models can then be used to predict the exact value of $\text{RMSE}(\tilde{\mathbf{r}})$ for every case. An example is shown in a later section of this paper.

Noise and Hodograph Size

Intuitively, the hodograph radius error due to circle fitting depends on the ratio between the circle's radius and the measurement noise. For the same radius, greater noise increases error. Conversely, for the same noise, a larger radius reduces error. The error in hodograph radius, therefore, could be related to the ratio between noise and circle radius:

$$\text{RMSE}(\tilde{R}) \propto \frac{\sigma}{R} \quad (41)$$

where σ is the noise and R is the radius of the circle. In the context of VIOD, σ is the standard deviation of velocity measurement noise and R is the radius of the orbit hodograph. 1000-sample Monte Carlo simulations were performed for a broad range of σ/R values in several orbit configurations; the results are shown in Figure 8.

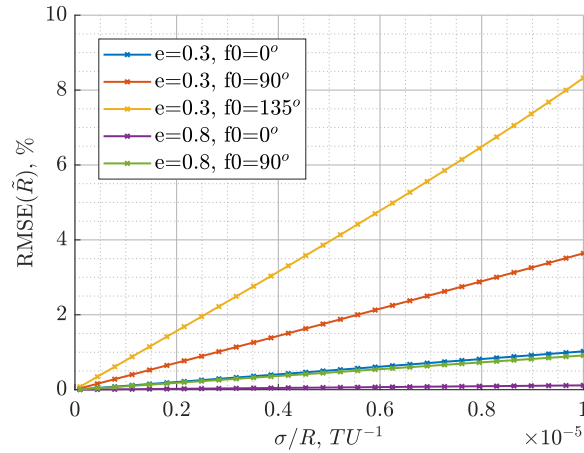


Figure 8. The hodograph circle fit error, $\text{RMSE}(\tilde{R})$, is shown as a function of the noise-to-velocity ratio σ/R for various orbit configurations.

It is clear that the relation in Eq. (41) holds true for a wide range of orbit configurations. Combining with the assumption made earlier in the section from Eq. (40) yields the relation between σ/R and VIOD error:

$$\text{RMSE}(\tilde{\mathbf{r}}) \propto \frac{\sigma}{R} \quad (42)$$

Since the diameter of the hodograph is the sum of the periaapsis and apoapsis velocities for an

elliptic orbit, the hodograph radius can be further expanded using the vis-viva equation as follows:

$$v_p = \sqrt{\frac{\mu}{a} \cdot \frac{1+e}{1-e}} \quad , \quad v_a = \sqrt{\frac{\mu}{a} \cdot \frac{1-e}{1+e}} \quad (43)$$

$$R = \frac{1}{2} (v_p + v_a) = \frac{1}{2} \sqrt{\frac{\mu}{a}} \left(\sqrt{\frac{1+e}{1-e}} + \sqrt{\frac{1-e}{1+e}} \right) = \frac{1}{2} \sqrt{\frac{\mu}{a}} \frac{2}{\sqrt{1-e^2}} = \sqrt{\frac{\mu}{a(1-e^2)}} \quad (44)$$

Eqs. (40) and (44) can be combined to express VIOD error trends as a function of σ , μ , a , and e :

$$\text{RMSE}(\tilde{\mathbf{r}}) \propto \sqrt{a(1-e^2)/\mu} \cdot \sigma \quad (45)$$

Finally, using canonical units defined in Eq. (37), Eq. (45) can be rewritten as:

$$\text{RMSE}(\tilde{\mathbf{r}}) \propto \sqrt{1-e^2} \cdot \sigma \quad (46)$$

Inspecting Eq. (44), it may seem unintuitive why the hodograph radius increases with higher eccentricity. This is because as eccentricity increases, the periapsis velocity of an elliptic orbit increases at a higher rate than the decrease of apoapsis velocity. As a result, the diameter of the orbit hodograph increases. The effect is illustrated in Figure 9 for further clarification.

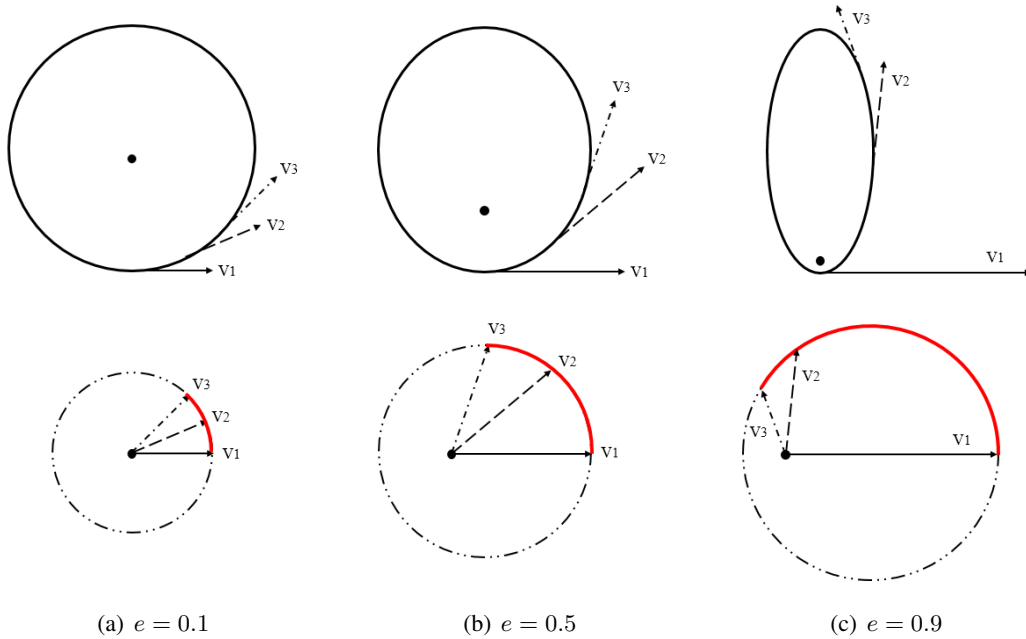


Figure 9. Three orbits with the same semi-major axis length and varying eccentricities (top row) have different orbit hodograph sizes (bottom row).

Measurement Arc Span

The circle fit radius error decreases when sample points are collected along a longer arc. Therefore the hodograph radius error should decrease when velocity measurements are taken along a greater portion of the orbit hodograph, in turn decreasing the VIOD error.

The arc measure between two points on the orbit hodograph is the true anomaly span Δf , as shown in Figure 1. To determine the relation between Δf and $\text{RMSE}(\tilde{R})$, 1000-sample Monte Carlo simulations of $\text{RMSE}(\tilde{R})$ as a function of Δf are performed for several orbits with different eccentricities. The results are shown in Figure 10.

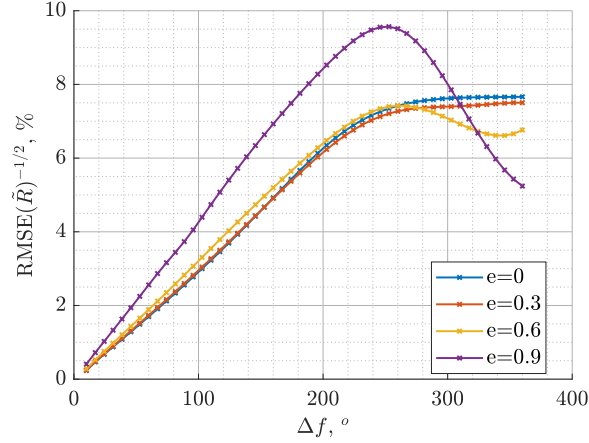


Figure 10. The inverse square root of $\text{RMSE}(\tilde{R})$ is plotted against the true anomaly span Δf for multiple orbits with different eccentricities.

It was found that Δf is nearly proportional to the inverse square root of $\text{RMSE}(\tilde{R})$ between 0° and 180° , as shown in Eq. (47). However, no clear trend exists beyond 180° . As a result, only measurements with $\Delta f < 180^\circ$ will be modeled for the remainder of the paper.

$$\text{RMSE}(\tilde{R}) \propto \Delta f^{-2}, \quad \Delta f < 180^\circ \quad (47)$$

The true anomaly span Δf is a function of the measurement interval, initial true anomaly, and eccentricity. The measurement interval is defined as the total time elapsed between the first and last velocity measurements. The initial true anomaly is the true anomaly at which the first velocity measurement is taken.

Intuitively, increasing the measurement interval increases Δf . Less intuitively, Figures 9 shows that the true anomaly span changes with eccentricity, and 11 illustrates how the true anomaly span is affected by the initial true anomaly. The following analysis shows how these parameters influence Δf analytically.

Assume n velocity measurements are taken at equal time intervals over a total interval of T for an orbit with semi-major axis a , eccentricity e , and initial true anomaly f_0 . To determine the true anomaly spanned by these measurements, begin by finding the initial mean anomaly, M_0 :

$$E_0 = 2 \arctan \left[\sqrt{\frac{1-e}{1+e}} \tan \frac{f_0}{2} \right] \quad (48)$$

$$M_0 = E_0 - e \sin E_0 \quad (49)$$

The ending mean anomaly can then be calculated as:

$$M_e = M_0 + \frac{T}{2\pi} \sqrt{\frac{\mu}{a^3}} \quad (50)$$

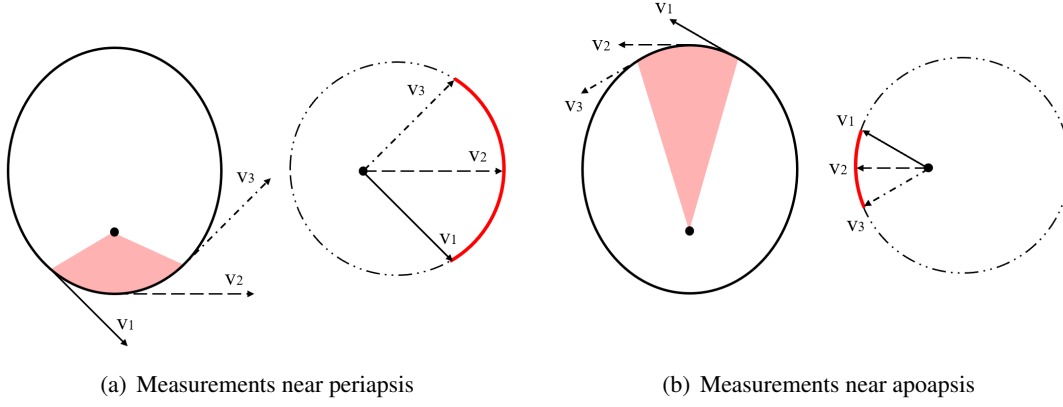


Figure 11. Over the same total time, velocity measurements near periapsis (a) span a greater arc on the orbit hodograph as compared to measurements near apoapsis (b).

Finally, the ending eccentric anomaly can be determined by solving Kepler's equation in Eq. (51) using Newton's method, and the true anomaly span can be recovered using Eqs. (52)-(53).

$$M_e = E_e - e \sin E_e \quad (51)$$

$$f_e = 2 \arctan \left[\sqrt{\frac{1+e}{1-e}} \tan \frac{E_e}{2} \right] \quad (52)$$

$$\Delta f = f_e - f_0 \quad (53)$$

To summarize, using Eqs. (48)-(53), the true anomaly span Δf can be calculated as a function of the measurement interval, eccentricity, and initial true anomaly. This process shall be referred to collectively as $\mathcal{F}(e, f_0, T)$:

$$\Delta f = \mathcal{F}(e, f_0, T) \quad (54)$$

Note that a and μ in Eq. (50) are not arguments to Eq. (54). This is because in canonical units, the term $\sqrt{\mu/a^3}$ is a constant. Then, combining Eqs. (40) and (47), the VIOD error trend can be expressed as a function of the true anomaly span:

$$\text{RMSE}(\tilde{\mathbf{r}}) \propto [\mathcal{F}(e, f_0, T)]^{-2} \quad (55)$$

ERROR MODEL VERIFICATION

The analytic models derived in the previous section are now verified using Monte Carlo simulations. The VIOD error, $\text{RMSE}(\tilde{\mathbf{r}})$, is assessed with respect to changes in the semi-major axis a , eccentricity e , initial true anomaly f_0 , and sensor noise standard deviation σ . $\text{RMSE}(\tilde{\mathbf{r}})$ data is collected from 3000-sample Monte Carlo simulations of 10 measurements taken at equal time intervals over 10% of the orbit period. Since the error trend models developed in this paper only reflect the proportionality encapsulated in the assumption in Eq. (40), they do not generate exact error values. The predicted error trends in the remainder of this section are scaled to match the range of the Monte Carlo data.

Verification: Semi-Major Axis

The relation between the semi-major axis a and $\text{RMSE}(\tilde{\mathbf{r}})$ as shown in Eq. (45) is compared with Monte Carlo simulations in Figure 12. In (a), (b), and (c), the maximum differences between the error model and Monte Carlo simulation results are 0.0004%, 0.005%, and 0.23%, respectively. This indicates that the analytic model matches closely with the simulations.

Note that VIOD error is much greater in (c), reaching over 80% as compared to less than 2.5% in (a). This is because the true anomaly spanned by the velocity measurements is extremely small near the apoapsis of highly eccentric orbits. While the error trend model can accurately predict error behavior, it would not be practical to use VIOD in such scenarios.

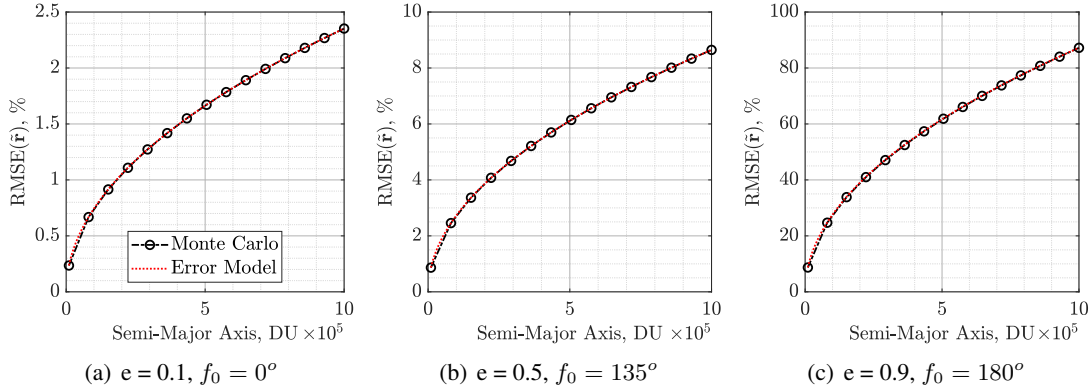


Figure 12. The VIOD error trend with respect to semi-major axis length as predicted by Eq. (45) is compared against Monte Carlo simulation results. Note the difference in y-axis scale between the three plots.

Verification: Eccentricity

The relationship between VIOD error trend and eccentricity is modeled by a combination of Eqs. (46) and (55):

$$\text{RMSE}(\tilde{\mathbf{r}}) \propto \frac{\sqrt{1 - e^2} \cdot \sigma}{[\mathcal{F}(e, f_0, T)]^2} \quad (56)$$

The eccentricity is varied between 0.1 and 0.9. Multiple initial true anomaly positions are studied as shown in Figure 13.

The difference in error trends in the three subplots arises from changes in the velocity vector. In (a), velocity measurements begin at periapsis. As the eccentricity is increased, velocities near periapsis increase, thus reducing the impact of sensor noise. In addition, the true anomaly spanned by measurements increases as illustrated previously in Fig 11, which improves the hodograph circle fit. Consequently, higher eccentricities yielded lower errors. In (c), the opposite phenomenon occurs: velocity decreases with higher eccentricities near apoapsis, and the true anomaly span decreases also. As a result, VIOD error increases with higher eccentricity. In (b), the true anomaly span decreases with eccentricity initially, but then increases at even higher eccentricities, resulting in an error plot resembling an inverted parabola.

The error trend model was able to capture all of the behavior described above, and matched Monte Carlo results to within 0.05%, 0.43%, and 0.08% for (a), (b), and (c), respectively.

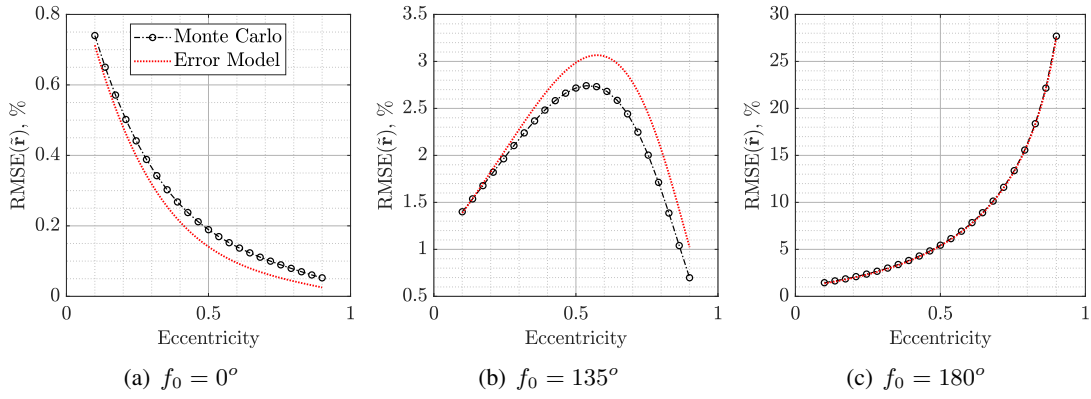


Figure 13. The VIOD error trend with respect to eccentricity as predicted by Eq. (56) is compared against Monte Carlo simulation results. Note the difference in y-axis scale between the three plots.

Verification: Initial True Anomaly

Eq. (55) models the relation between VIOD error trends and the initial true anomaly. The initial true anomaly is varied between 0° and 360° for orbits with different eccentricities as shown in Figure 14. Note that the error trends become sharper as eccentricity increases: this is because highly eccentric orbits have low velocities and small true anomaly spans near apoapsis, which causes VIOD error to rise rapidly as the initial true anomaly approaches 180° . The error trend model is able to capture this trend, and the maximum difference between the model and Monte Carlo simulation results were 0.12%, 0.32%, and 1.23% for (a), (b), and (c), respectively.

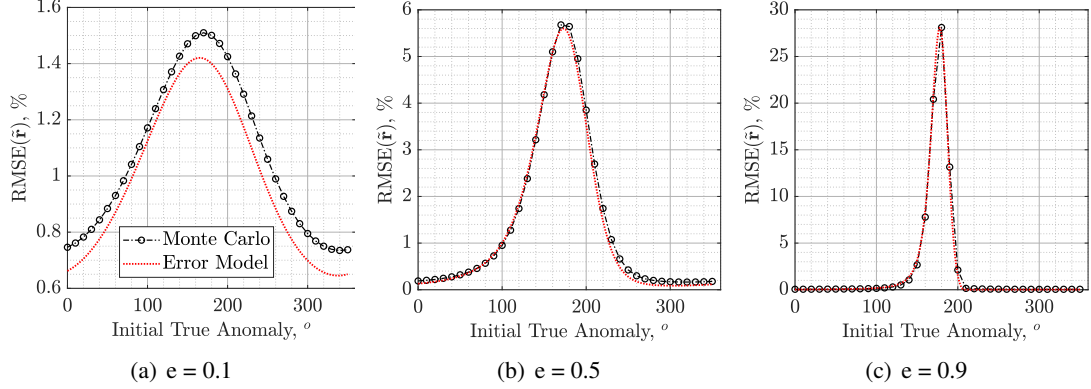


Figure 14. The VIOD error trend with respect to starting true anomaly change as modeled by Eq. (55) is compared against Monte Carlo simulation results. Note the difference in y-axis scale between the three plots.

Verification: Sensor Noise

VIOD error trends and sensor noise are related by Eq. (46). Sensor noise is varied between 5×10^{-7} DU/TU and 1×10^{-5} DU/TU for three scenarios with varying eccentricity and initial true anomaly, shown in Figure 15. The analytic model was able to match Monte Carlo simulation results within 0.04%, 0.26%, and 1.51% for (a), (b), and (c), respectively.

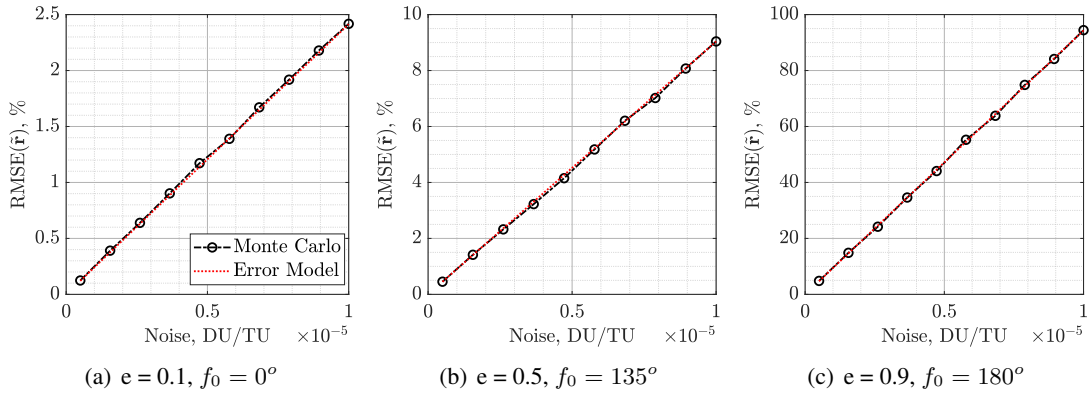


Figure 15. The VIOD error trend with respect to sensor noise as modeled by Eq. (46) is compared against Monte Carlo simulation results. Note the difference in y-axis scale between the three plots.

EXAMPLE: PREDICTING THE ERROR OF AN EARTH-NEPTUNE TRANSFER ORBIT

Since the error trend model only reflects the proportionality of VIOD errors with respect to changes a , e , f_0 , and σ , it cannot generate an exact error value for any particular case. However, if $\text{RMSE}(\tilde{\mathbf{r}})$ is known for any case, the error trend model can then be used to predict the exact error for every case. In this section, the $\text{RMSE}(\tilde{\mathbf{r}})$ of a target orbit will be predicted by applying error trend models to the known RMSE error of a reference orbit.

An Earth-Neptune transfer orbit is chosen as the target orbit. VIOD uses velocity, not position data, which allows VIOD to leverage non-Earth-based measurement techniques such as XNAV. Thus the accuracy and practicality of VIOD is not constrained by the distance to Earth, which makes VIOD particularly suited for deep space navigation, such as to the outer planets. As such, an Earth-Neptune transfer orbit can be a practical scenario for VIOD applications.

Reference and Target Orbits

The reference orbit can be arbitrarily chosen. For this example, a reference orbit with $a^* = 1 \times 10^5$ DU, $e^* = 0.5$, and $f_0^* = 90^\circ$ is used. 10 measurements are taken at equal time intervals over 10% of the orbit period with sensor noise $\sigma^* = 3 \times 10^{-5}$ DU/TU. A Monte Carlo simulation run with 3000 samples is used to determine the error of the reference orbit. Simulation results are shown in Figure 16. The reference orbit's RMSE is determined to be $\text{RMSE}(\tilde{\mathbf{r}})^* = 7.23\%$.

The target orbit is an Earth-Neptune transfer orbit with $a = 15.53$ AU and $e = 0.9356$. The initial measurement is taken near Neptune at $f_0 = 170^\circ$. Sensor noise standard deviation is set to 5 m/s, and 10 measurements are taken over 10% of the orbit period. The parameters are then converted to canonical units using Eqs. (37) and (38), yielding sensor noise $\sigma = 2.09 \times 10^{-6}$ DU/TU. The parameters of the reference orbit and the Earth-Neptune orbit are summarized in Table 3.

Table 3. Summary of parameters for the reference orbit and the Earth-Neptune transfer orbit.

	a (DU)	e	f_0 ($^\circ$)	σ (DU/TU)
Reference	1×10^5	0.500	90	3.00×10^{-5}
Earth-Neptune	1×10^5	0.936	170	2.09×10^{-6}

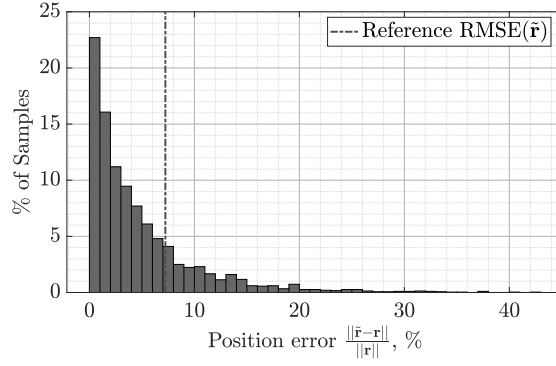


Figure 16. Histogram of VIOD position error for the reference orbit from a 3000-sample Monte Carlo simulation.

Error Conversion Using VIOD Error Trends

The VIOD error trend is modeled by the hodograph via Eqs. (46) and (55). Since a reference error and its hodograph is known, the error of the desired orbit can be computed by the following:

$$\frac{\text{RMSE}(\tilde{\mathbf{r}})}{\text{RMSE}(\tilde{\mathbf{r}})^*} = \frac{\sigma}{\sigma^*} \cdot \frac{\sqrt{1-e^2}}{\sqrt{1-e^{*2}}} \cdot \left[\frac{\mathcal{F}(e^*, f_0^*, T^*)}{\mathcal{F}(e, f_0, T)} \right]^2 \quad (57)$$

The predicted error for the Earth-Neptune transfer orbit is calculated to be 15.39%. In comparison, a 3000-sample Monte Carlo simulation of the same orbit yielded an error of 15.01%, shown in Figure 17. This indicates that the error trend model is successful in predicting the error of an orbit using a different, arbitrary reference orbit.

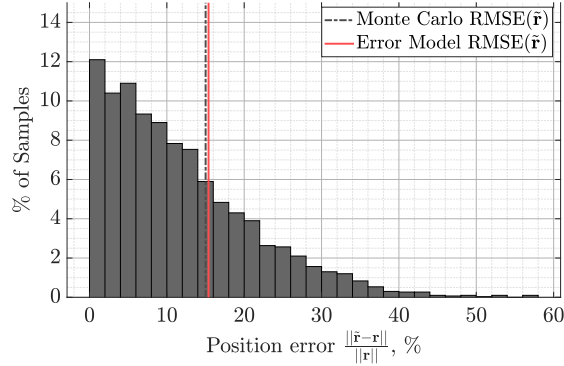


Figure 17. Histogram of VIOD position error for the Earth-Neptune transfer orbit from a 3000-sample Monte Carlo simulation. The vertical lines show $\text{RMSE}(\tilde{\mathbf{r}})$ values calculated from the Monte Carlo simulation and predicted by the error model.

CONCLUSION

An improved velocity-based initial orbit determination algorithm was proposed and demonstrated to be more accurate and computationally efficient than previous VIOD algorithms. With the improved algorithm, VIOD error trends were analytically modeled by using the orbit hodograph to relate changes in orbit parameters with position error. The error trend models were validated using Monte Carlo simulations. An example case of an Earth-Neptune transfer orbit was provided to demonstrate how the error trend models can be used to predict VIOD error.

NOMENCLATURE

General

VIOD	velocity-based initial orbit determination
RMSE	root mean square error
μ	gravitational parameter of the central body
a	semi-major axis
\mathbf{e}	eccentricity vector
i	inclination
Ω	longitude of ascending node
ω	argument of periapsis
f	true anomaly
f_0	initial true anomaly
E	eccentric anomaly
M	mean anomaly
\mathbf{k}	unit vector orthogonal to the orbital plane
\mathbf{h}	angular momentum vector
\mathbf{r}_i	the true i^{th} position vector
$\tilde{\mathbf{r}}_i$	VIOD estimate of \mathbf{r}_i
\mathbf{v}_i	the true i^{th} velocity vector
$\tilde{\mathbf{v}}_i$	\mathbf{v}_i , perturbed by sensor noise η_i
η_i	sensor noise vector for the i^{th} measurement
$\hat{\eta}$	unit vector of η
σ	sensor noise standard deviation
DU	canonical distance unit
TU	canonical time unit
R	radius of the hodograph
\tilde{R}	circle fit estimate of the hodograph radius
n	number of velocity measurements

Energy Method

\mathbf{u}_i	unit vector of \mathbf{v}_i
\mathbf{w}_i	unit vector orthogonal to \mathbf{k} and \mathbf{u}_i
\mathbf{r}_{u_i}	component of \mathbf{r}_i in the direction of \mathbf{u}_i
\mathbf{r}_{w_i}	component of \mathbf{r}_i in the direction of \mathbf{w}_i

Hodograph Method

\mathbf{u}_x	unit vector orthogonal to \mathbf{k} and \mathbf{v}_i
\mathbf{u}_y	unit vector orthogonal to \mathbf{k} and \mathbf{u}_x
\mathbf{T}_O^I	rotation matrix from inertial frame to orbit frame
\dot{x}_{O_i}	x-coordinate of \mathbf{v}_i in the orbit frame
\dot{y}_{O_i}	y-coordinate of the \mathbf{v}_i in the orbit frame
(\dot{x}_c, \dot{y}_c)	center of the hodograph in the orbit frame
\mathbf{c}	center of the hodograph in the inertial frame
\mathbf{u}_{\perp_i}	unit vector perpendicular to \mathbf{r}_i
\mathbf{u}_{\parallel_i}	unit vector parallel to \mathbf{r}_i
ρ_i	magnitude of \mathbf{r}_i

Improved Method

\mathbf{A}	parameter vector for the equation of a circle
\mathbf{Z}	data matrix
\mathbf{M}	matrix of moments
η	Lagrange multiplier
\mathcal{G}	objective function

REFERENCES

- [1] J. A. Christian and C. L. Hollenberg, “Initial orbit determination from three velocity vectors,” *Journal of Guidance, Control, and Dynamics*, Vol. 42, No. 4, 2019, 10.2514/1.G003988.
- [2] C. L. Hollenberg and J. A. Christian, “Geometric Solutions for Problems in Velocity-Based Orbit Determination,” *Journal of the Astronautical Sciences*, Vol. 67, mar 2020, 10.1007/s40295-019-00170-7.
- [3] J. Prussing and B. Conway, *Orbital Mechanics*. Oxford University Press, 2012.
- [4] J. Branham, R. L., “Laplacian Orbit Determination,” *Astronomy in Latin America* (R. Teixeira, N. V. Leister, V. A. F. Martin, and P. Benevides-Soares, eds.), Vol. 1, Nov. 2003.
- [5] L. G. Taff, “On Initial Orbit Determination,” *The Astronomical Journal*, Vol. 89, Sept. 1984, 10.1086/113644.
- [6] H. D. Curtis, “Chapter 5 - Preliminary Orbit Determination,” *Orbital Mechanics for Engineering Students (Second Edition)*, pp. 255 – 317, Boston: Butterworth-Heinemann, 2010.
- [7] R. Gooding, “A new procedure for orbit determination based on three lines of sight (angles only),” tech. rep., Defence Research Agency Farnborough (United Kingdom), 1993.
- [8] S. I. Sheikh, D. J. Pines, P. S. Ray, K. S. Wood, M. N. Lovellette, and M. T. Wolff, “Spacecraft navigation using X-ray pulsars,” *Journal of Guidance, Control, and Dynamics*, Vol. 29, No. 1, 2006.
- [9] A. Al-Sharadqah and N. Chernov, “Error analysis for circle fitting algorithms,” *Electronic Journal of Statistics*, Vol. 3, 2009, 10.1214/09-EJS419.
- [10] N. Chernov and C. Lesort, “Least Squares Fitting of Circles,” *Journal of Mathematical Imaging and Vision*, Vol. 23, 2005, 10.1007/s10851-005-0482-8.
- [11] S. Eliassi, “GitHub - Circle-Fitting-Hyper-Fit,” 2017. <https://github.com/SohranEliassi/Circle-Fitting-Hyper-Fit>, Last accessed on 2020-08-06.